CCFE
CULHAM CENTRE FOR FUSION ENERGY

UK Atomic Energy Authority

UKAEA-CCFE-PR(23)171

Pui-Wai Ma, Daniel R. Mason, Steven Van Boxel,
Sergei L. Dudarev

Evolution of nanocrystalline tungsten at low temperature due to irradiation-induced strains

Evolution of nanocrystalline tungsten at low temperature due to irradiation-induced strains

Pui-Wai Ma, Daniel R. Mason, Steven Van Boxel, Sergei L. Dudarev

This is a preprint of a paper submitted for publication in Materials Research Letter

Evolution of nanocrystalline tungsten at low temperature due to irradiation-induced strains

Pui-Wai Ma[a], Daniel R. Mason[a], Steven Van Boxel[a], and Sergei L. Dudarev[a]

[a]United Kingdom Atomic Energy Authority, Culham Science Centre, Abingdom, Oxfordshire, OX14 3DB, United Kingdom

ARTICLE HISTORY
Compiled December 7, 2022

ABSTRACT
We simulate effects of irradiation on nanocrystalline tungsten in the athermal high dose limit using the creation-relaxation algorithm, where microstructural evolution is driven not by thermally activated diffusion, but by fluctuating stresses resulting from the production and relaxation of defects. Over the entire interval of radiation exposure spanning several dpa, samples with smaller grains swell less than those with larger grains, featuring defect denuded zones resulting from the continuously fluctuating atomic configurations at grain boundaries. The grain size distribution broadens as a function of exposure, and the average grain size increases due to coarsening of grain microstructure if a low visibility criterion is applied to small grains.

KEYWORDS
Nanocrystals; tungsten; irradiated materials; microstructure evolution; swelling

Graphical Abstract

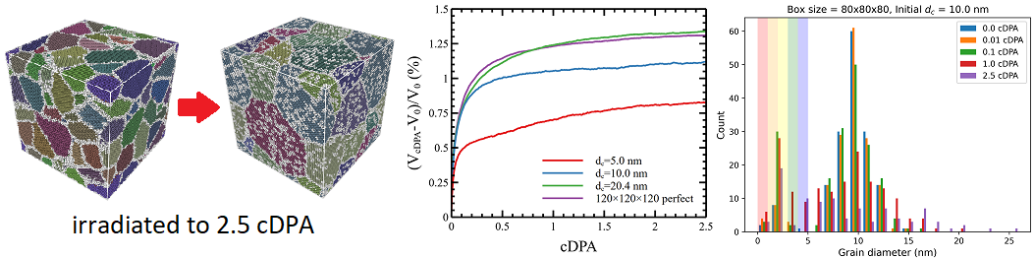

IMPACT STATEMENT

In the absence of thermal diffusion, grain boundaries in a nanocrystalline material reduce radiation swelling. Grain size distribution broadens, suggesting that the evolution of a nanocrystalline material under irradiation involves a variety of dynamic processes not amounting only to grain coarsening.

CONTACT Pui-Wai Ma. Email: Leo.Ma@ukaea.uk

1. Introduction

High-energy neutrons, generated by the nuclear fuel in a fission reactor or by the deuterium-tritium plasma in a fusion device, undergo multiple scattering and propagate over several tens of centimetres in reactor materials [1]. Elastic and inelastic interactions of energetic neutrons with atomic nuclei give rise to atomic recoils [2], initiating collision cascades that in a perfect crystal produce readily identifiable structural defects, primarily dislocation loops and vacancy clusters [3–6]. The accumulation of these defects degrades thermal [7–9] and mechanical [10,11] properties of materials, giving rise to swelling [12,13] and dimensional changes [14].

The fact that microstructurally complex materials exhibit greater stability under irradiation is well recognised. For example, ferritic-martensitic steels show far greater resistance to radiation swelling than pure alloys with similar chemical compositions [15,16]. Nanocrystalline (NC) materials are another notable class of materials with complex microstructure, characterised by a large grain boundary (GB) interface to volume fraction [17]. The acknowledgment of a potentially beneficial role of GBs stimulated research in nanostructural materials exposed to irradiation [18,19]. At high temperatures, where defects migrate by thermal activation, they can be absorbed and annihilated at GBs [20], resulting in the formation of zones of lower defect density near GBs observed in irradiated materials [21]. Experiments [19,22] show that indeed the average density of radiation defects in NC and ultra-fine grain materials is significantly lower than in coarse-grained samples. The phenomenon is observed in NC metals and insulators [23,24], suggesting that the defect formation suppression effect is generic and associated solely with high GB density. Mathematical analysis of interaction of defects with GBs, where the latter were represented by dislocation arrays and where defects were assumed to perform thermally activated diffusion [25], explains the variation of the density of defects as a function of grain size.

Atomic scale simulations help understand the nature of interaction between an individual GB and radiation defects [26–30]. Simulations show that a GB is not a static sink for defects but rather a dynamically evolving region, altering its configuration in the process of absorption or emission of a defect. GB can emit interstitial atom defects to annihilate vacancies nearby [27], whereas the annihilation of defects at a GB is a collective process involving the rearrangement of positions of many atoms [30]. Fluctuating motion of GBs in copper under irradiation [28,29] results in that stacking fault tetrahedron (SFT) defects are incorporated in GBs through collective many-atom reactions, driven by the free energy minimisation.

Fluctuations of GB structure, whether thermal or athermal - i.e. driven solely by irradiation - are expected to give rise to the coarsening of grain microstructure [31]. The coarsening of grain microstructure under irradiation was observed and extensively studied experimentally [31–34]. Initially, Wang *et al.* [32] assumed that the average diameter of grains varied linearly as a function of radiation exposure. Further studies showed that in the higher dose limit, the rate of grain growth slows and becomes sub-linear [33,34]. Kaoumi *et al.* [31] developed a model, based on Vineyard's thermal spike concept [35], that predicts that in the athermal limit the variation of the average grain size $\bar{d}_g$ as a function of dose ϕ follows a cubic polynomial law $\bar{d}_g{}^3(\phi) - \bar{d}_g{}^3(0) \propto \phi$. This functional form appears to provide a good fit to the available experimental data, but it has not yet been established if this model is consistent with direct atomistic simulations.

There are very few parameter-free theoretical studies of NC materials in the limit of high exposure to irradiation. Levo *et al.* [36] performed collision cascade simulations

in NC nickel and multicomponent alloys, observing the occurrence of grain coarsening. However, the high computational cost of collision cascade simulations results in that even the most advanced analysis [37] proves difficult to extend beyond the dose of 1 dpa.

Below, we explore the evolution of microstructure of a NC material in the high dose limit using a parameter-free atomistic creation-relaxation algorithm (CRA) [38]. CRA simulations apply in the temperature range where thermal diffusion of defects, primarily vacancies, is ineffective, making the predicted pattern of evolution pertinent to steels and zirconium alloys in the temperature range below 300°C [38,39] and to nominally pure tungsten below approximately 700°C [38,40]. CRA is conceptually similar to the Frenkel Pair Accumulation (FPA) algorithm [41] used in the analysis of formation of C15 clusters and their transformation into $\frac{1}{2}\langle 111\rangle$ and $\langle 100\rangle$ dislocation loops in iron. Extensive comparison of microstructures observed in ion irradiation experiments on tungsten with CRA simulations shows good agreement between theoretical predictions and experimental observations [42].

In what follows, we simulate swelling and microstructural evolution of heavily irradiated NC tungsten. Tungsten is the plasma facing material selected for ITER and DEMO fusion devices [43,44]. By extending the simulations into the interval of high dose, previously inaccessible to a direct computational analysis, we find that the relationship between the grain size and swelling rate stems from the reduction of defect content in the vicinity of GBs. We explore the fluctuating dynamics of evolution of GBs as a function of radiation exposure, and conclude that thermally activated diffusion is not necessarily responsible for the experimentally observed formation of GB defect denuded zones, which in our simulations emerge as a result of stress-driven fluctuating evolution of GB structures.

2. Simulation setup

Simulation cells with equiaxed grains were generated using the Voroni tesselation method with the ATOMSK code [45]. Voronoi polyhedra were filled with atoms in a body-centred-cubic (bcc) structure with random crystallographic orientations. ATOMSK then removes atoms until none has a neighbour within 2 Å. We created 6 sets of simulation cells. Initial samples have a characteristic grain diameter d_c of 5.0, 7.5, 10.0, and 12.7 nm in a cubic cell with dimensions equivalent to $80 \times 80 \times 80$ bcc unit cells with the supercell side length of 25.144 nm, and 15.1 and 20.4 nm in a cubic cell with dimensions equivalent to $120 \times 120 \times 120$ bcc unit cells with the supercell side length of 37.716 nm. d_c is the diameter of a sphere with the same volume as an average grain. We also created cells with perfect crystal structure. All the results shown below are averaged across 5 independent samples from each set of simulations.

Our preparation method for relaxing the NC starting configurations is similar to that described in Ref. [38]. Firstly, we relax an atomic configuration using conjugate gradients, followed by thermal relaxation at 300K for 1 ns. Then, we allow the cells to change their volumes and shapes to achieve stress-free conditions, and run MD simulations for further 1 ns. The temperature is linearly reduced from 300K to 0K during the second stage of the simulation. Finally, the cell and atomic configuration are relaxed using conjugate gradients again. All the simulations were performed using LAMMPS [46,47], and the Marinica EAM4 [48] as well as the Mason-Nguyen-Manh-Becquart (MNB) interatomic potentials [49]. The results are qualitatively similar, exhibiting some quantitative differences, where typically a more dense defect distribution is found

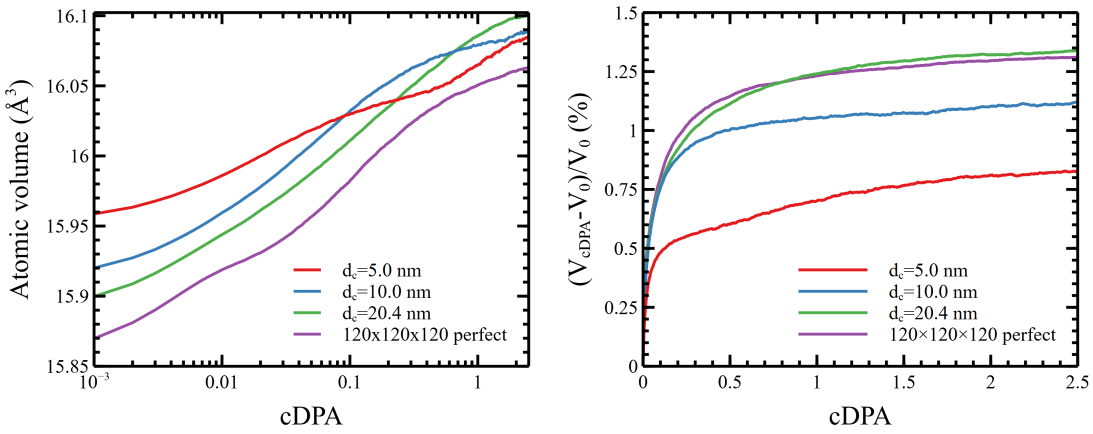

Figure 1. Average atomic volume and the relative volume with respect to the initial volume as a function of dose in unit of cDPA.

using EAM4, in agreement with other studies. For the clarity of exposition, we only present the data produced using the MNB potential.

The microstructure of samples evolves as a function of canonical displacements per atom (cDPA) according to CRA. We use the unit cDPA to distinguish it from the conventional definition of NRT-DPA [50]. A Frenkel pair is created by moving a randomly-selected atom to a random position. In each CRA step, we create n Frenkel pairs, followed by energy minimisation using the conjugate gradient method. One can accumulate the dose of n/N cDPA at each step, where N is the total number of atoms in the simulation cell. Atomic configurations evolve according to the resulting spatially heterogeneous energy landscape.

CRA is an extremely computationally efficient method, as it does not consider thermal excitation, hence no true diffusion is involved in the simulated evolution of microstructure. However, mass transport can still happen, since an interstitial can have a low energy barrier [51] which can be overcome by local stresses alone. CRA is therefore an important method for detecting and determining physically-relevant stress-driven processes. CRA gives an upper bound of resulting defect density, and is directly comparable to experiment in the low-temperature limit, or when activation processes are hindered by impurities, present in any conventionally manufactured material.

To identify grains and GB properties, we use the method described in the supplementary material, see section 4.

When dealing with polycrystalline configurations, one cannot use the Wigner-Seitz analysis to identify vacancies and self-interstitial atoms, as the reference lattice is changing. Recently, Mason *et al.* [52] developed a new void detection method requiring only the local lattice orientation and applicable to heavily irradiated materials. We do not yet have a good method to identify self-interstitial atoms in a heavily irradiated polycrystalline configuration. In the context of swelling, the increase in the global excess volume due to the displaced atoms is best identified by counting vacancies and voids.

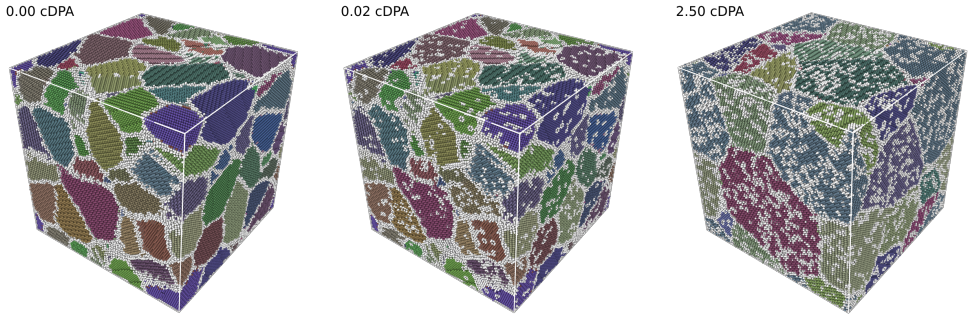

Figure 2. A sample initialised with 71 grains and d_c=7.5nm at different doses. Grains are determined by OVITO using the grain segmentation modifier. Atoms are coloured according to crystal orientations. Non-bcc atoms are colored in white.

3. Results and discussion

Fig. 1 shows a key finding that samples with smaller grains appear more resistant to radiation-induced swelling. It shows the change of the average atomic volume and relative volume of systems with different initial grain sizes as a function of dose. Perfect crystal case is also shown for comparison. Systems with smaller grains have a larger atomic volume prior to irradiation. The excess volume is due to the non-crystalline arrangement of atoms in the GB. The atomic volume increases as defects accumulate. At high dose the relative increase is lower for the smaller grain samples. If we examine the relative volume change of the simulation cell, systems with smaller grain sizes exhibit lower swelling than larger grain samples or the single crystal.

We can understand this phenomenon as a combined contributions relating to the change of GB area and the change of vacancy & void (v+v) concentration. First, we examine the GB area aspect. Fig. 2 shows a sample with initial d_c=7.5 nm, at different radiation exposures. Both the defects and GB nanostructures evolve and change significantly as a function of dose, graphically illustrating that GBs do not behave as static sinks that remain stationary in real space. GBs interact with defects, evolve, and fluctuate. The change of shape and coarsening of grains can be observed as the dose increases.

Our results are consistent with the work by Levo *et al.* [36], who performed collision cascade MD simulations of NC nickel and nickel-based multi-components alloys with grain size of 10 nm, observing similar grain coarsening. Our results are also in line with the studies performed in Refs. [18,26–30] showing that GBs interact with defects and change morphology as a result of local atomic rearrangement.

To examine the change of the number of grains and GB area quantitatively, we plotted them in Fig. 3 as a function of dose. For small grain samples, the numbers of grains decreases rapidly as a function of dose, whereas samples with larger grain sizes show a markedly smaller decrease in count. Samples appear to be experiencing grain coarsening. The GB area per volume drops, especially when the initial grain size is small. Therefore, the excess volume due to the GBs decreases. It is the first aspect that counteracts the increase of average atomic volume due to the accumulation of defects.

Do the grains really coarsen? We can observe the change of grain size distribution as experiments do by plotting histogram in Fig. 4. The grain diameter d_g is calculated from each grain volume assuming a spherical shape. For systems with initial d_c= 5.0

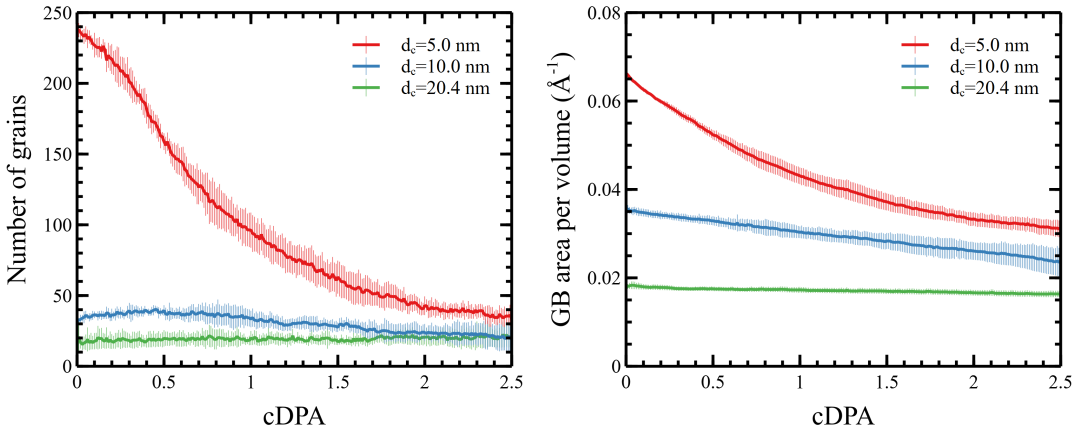

Figure 3. Number of grains and grain boundary area per volume as a function dose. Error bars are the standard deviation across 5 samples.

nm, a clear pattern of grain coarsening can be observed. While for larger grain systems, the size distributions show broadening instead. Not only large grains can be observed above 1.0 cDPA, we can see small grains forming. A grain is defined as a group of atoms with neighbourhood sharing similar crystal orientation, while in our algorithm we used a cutoff of 100 atoms as the smallest size of a grain, corresponding to d_g 1.4 nm. It is arguably for the increasing numbers of grains with $d_g < 1.4$ nm being a results of increasing numbers of very small fragments produced by irradiation and considered collectively as small grains. On the other hand, we can clearly see an increment of small grains with d_g in the range between 2 to 5 nm.

By inspecting the histograms summarising the results of ion irradiation [32,34] and neutron irradiation [53] experiments, one could deduce the visibility limit of grains of about 5nm. We shaded the histogram of grain sizes derived from simulations by different colours for each 1 nm increment. As the visibility decreases, small grains are gradually eliminated from the analysis. This procedure recovers the size distribution generally observed in experiments where only large grains are observed that form at high dose. Although we can see numerous small grains, for the initial size $d_c \geq 10.0$ nm, the total volume of grains smaller than 5 nm at all doses is lower than 1% of the total, which is negligible. In the actual observations, such small grains may easily be confused with a part of GB structure and ignored.

Grain coarsening usually involves the variation of the average grain diameter. Ion irradiation experiments [54] suggest that $\bar{d_g}^n(\phi) - \bar{d_g}^n(0) \propto \phi$, where $1.9 < n < 4.3$. Kaoumi *et al.* [31] developed a thermal spike model predicting that $n = 3$, in agreement with experimental observations. Neutron irradiation of NC copper [53] also indicates a sublinear increment of average d_g as a function of dose. However, we note that either the grain visibility in experiment or the cutoff diameter in a simulation would affect the counting and identification of grains. This also implies that the average grain diameter is a quantity that can vary due to subjective interpretation.

In Fig. 5, we plotted the average d_g as a function of dose, but discarding grains with diameters smaller than 2.5 nm and 5 nm. We can observe for smaller grains system that the average grain diameter increases in both cases. While for $d_c > 10$ nm, it depends on the cutoff diameter. However, we don't observe any increase according to the power relation. This may be due to the inhibited interstitial atoms diffusion in CRA, while the thermal spike model rely on the atomic jump due to local heating.

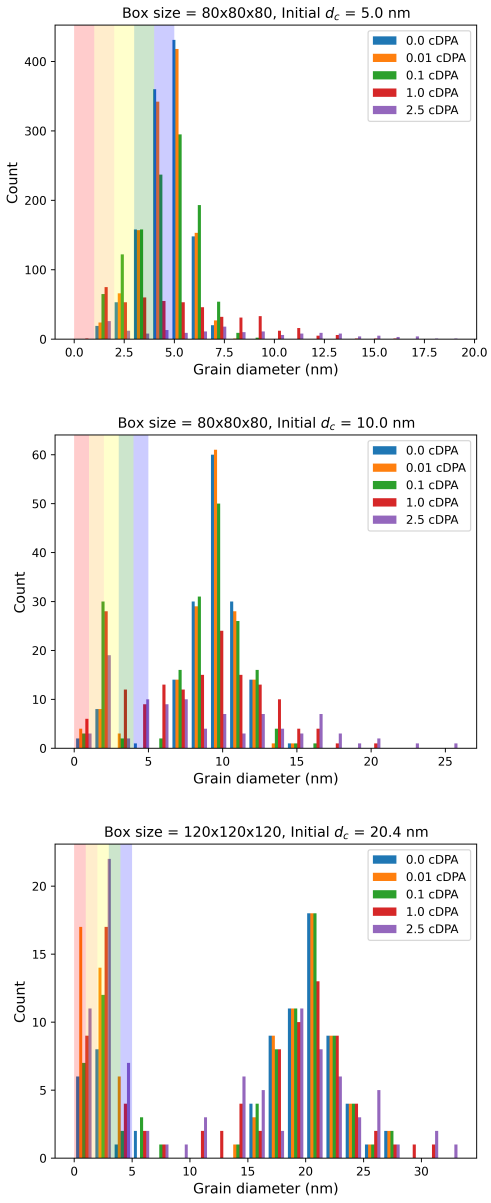

Figure 4. Histogram of grain diameter at difference dose. The grain diameter is calculated from the grain volume assuming a spherical shape. Shaped areas represent varying levels of visibility in experiments.

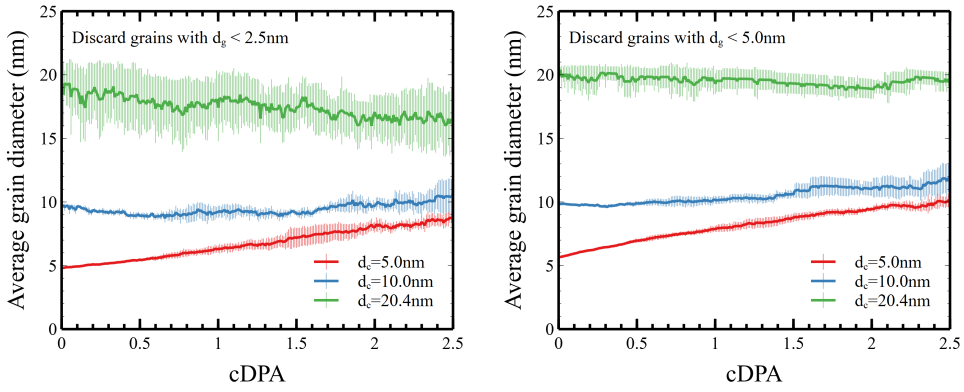

Figure 5. The average grain diameter as a function of dose by discarding grains with d_g smaller than 2.5 nm and 5.0 nm.

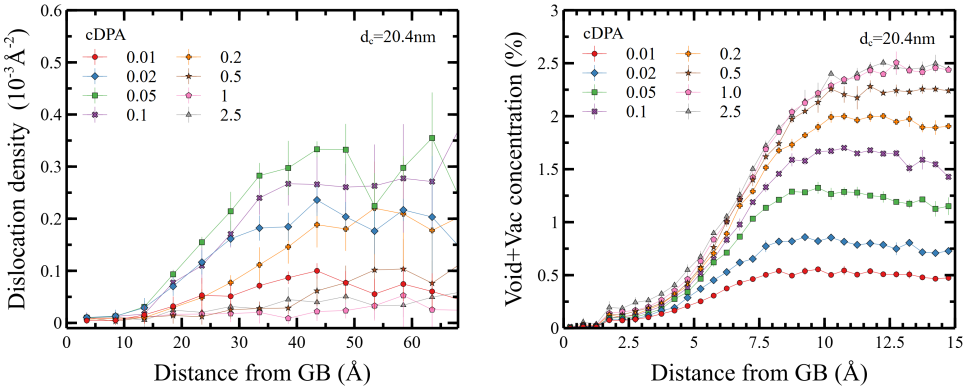

Figure 6. Dislocation density and void concentration as a function of distance from the grain boundary.

Barr *et al.* [55] compared the GB roughening and migration occurring due to collision cascade impacts, local melting and FPA simulations. GB migration is more visible in collision cascade and local melting simulations, which involve the long term point defects production and annealing.

Other than grain coarsening, we now examine how GB-defect interaction may affect defect production, especially the v+v concentration, that affect the swelling. This requires understanding the spatial distribution of defects in the presence of GBs. A new algorithm was developed (see Appendix) such that one can define the instantaneous configuration of GBs as a triangulated surface. Then, we can compute the distance of each atom to each triangle, and so find the minimum distance from each atom to a GB. Using this measure we can plot properties as a function of distance to a GB.

Fig. 6 shows the dislocation density and v+v concentration as a function of distance from the GB. The dislocation density is calculated as follows. First, we remove atoms with the distance from a GB that is smaller than D. Then, we perform the dislocation analysis (DXA) following Ref. [56]. This gives the dislocation line length (L_D). We say the dislocation density at D is $(L_{D-\delta} - L_{D+\delta})/(V_{D-\delta} - V_{D+\delta})$, where V_D is the corresponding volume. We used $\delta = 2.5$Å here. As low-angle GBs can be interpreted as arrays of dislocations, we exclude atoms within 1 Å of a GB from the analysis. For the v+v concentration, instead of removing atoms, we consider atoms with distance from GB incrementally. Then, we calculate the v+v volume within a volume defined

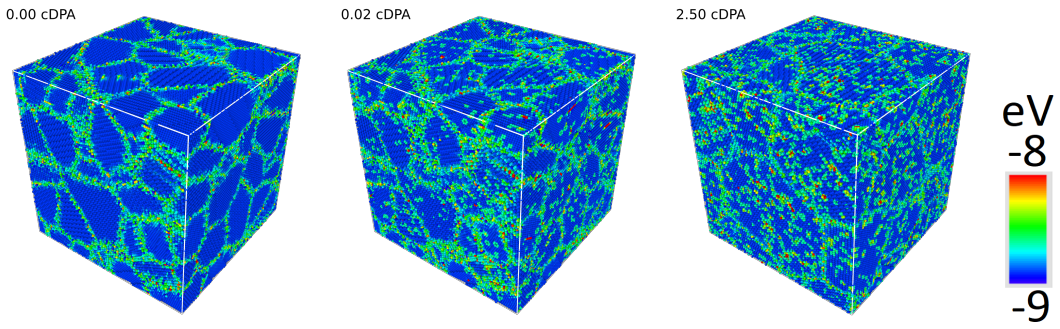

Figure 7. Atoms are coloured according to their atomic potential energies in unit of eV. The same sample as in Fig. 2.

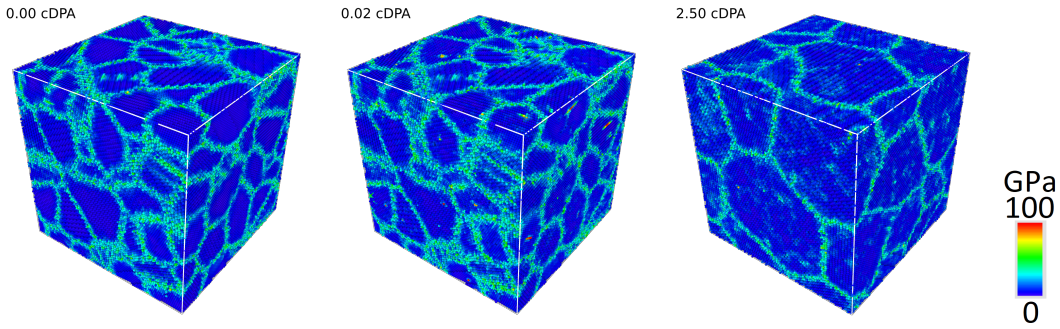

Figure 8. Atoms are colored according to their von Mises stress in unit of GPa.The same sample as in Fig. 2.

by the distance from GB. Using a similar finite difference method, we can find the v+v concentration within a volume corresponding to an interval of 0.5 Å. We should note the results from distance zero to about a lattice constant are unreliable, since the algorithm is unable to find full size vacancies at the GB surfaces.

We can clearly observe that both the dislocation density and v+v concentration are reduced near the GB. While on a short length scale of a few lattice parameters, this is a clear signature of a denuded zone. Since vacancy and void are the main contribution to swelling, with vacancy and voids suppressed near GB, the total v+v concentration is lower than in a perfect crystal. This is the second aspect making NC materials more irradiation swelling resistant.

We now inspect the correlation between the spatial defect distribution and the potential energy, as well as the von Mises stress (VMS). As the microstructure evolves, the spatial potential energy landscape changes. Fig. 7 shows the spatial distribution of atomic potential energy of the same sample as in Fig. 2. We observe higher potential energy at the GBs initially. As damage accumulates, more atoms attain high potential energy. If we compare this to Fig. 2, we can see that the high potential energy regions are the locally non-bcc defect structures. If we examine the spatial distribution of von Mises stress (VMS) in Fig. 8, VMS is higher at the GBs. Defects give a smaller contribution to VMS compared to GBs.

In Fig. 9, we plotted the average atomic potential energy and the average VMS as a function of distance from a GB. At small distances, where atoms are close to the GB surface, the potential energy is high. Before irradiation, energy drops smoothly to the bulk value beyond 10 Å. As the dose increases, the potential energy increases inside

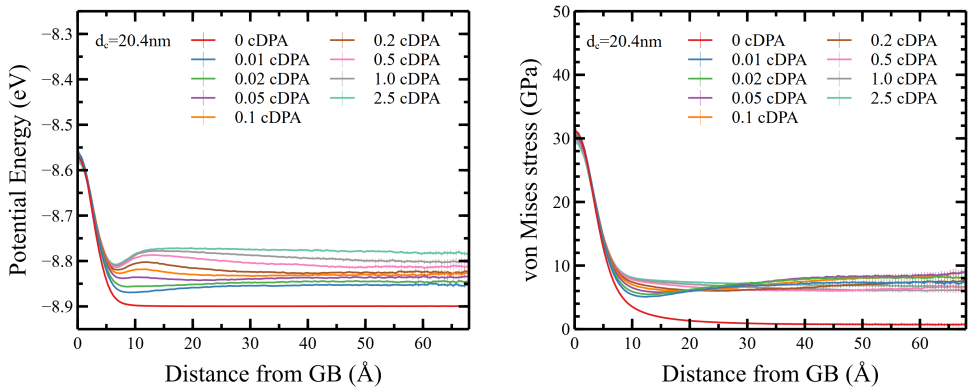

Figure 9. Average atomic potential energy and average von Mises stress as a function of distance from the grain boundary. The initial $d_c = 20.4$ nm.

the grains. However, the potential energy does not rise so rapidly at the GB. At large dose, we can observe a clear minimum at around 7 Å (about two lattice parameters). In the case of VMS, the overall picture is similar. We can observe that at distance zero, VMS decreases as the dose increases. Irradiation relaxes the stress at the GB. At high dose, a minimum at about 12 Å can be observed.

It appears that the minima are correlated with elastic fields due to the distorted microstructure at the GB and the accumulation of damage inside the grain, which superimpose in the defects denuded zone. Since the corresponding change of elastic energy landscape is quadratic in the elastic stress field, we would expect the positions of the minima to be different for the potential energy and stress.

What is the origin of such seemingly denuded zone for defects in the absence of diffusion? What is the mechanism of grain coarsening driven by irradiation? Indeed, these two questions can be answered as one. They are both resulting from the movement or fluctuation of the GB structure due to the GB-defect interactions. When GBs and defects interact, since both are at higher energy and unstable, lower energy configuration is attained after the relaxation of atomic environment. The local lattice distortion, which causes high stress concentration, can drive the rearrangement of atomic configurations [38–40,57]. Defects near the GB are absorbed and incorporated as part of the GB. This changes the morphology of GB, and the process itself has a clear signature of a local structural fluctuation.

Fig. 10 shows snapshots of the VMS in a sample from 2.515 cDPA to 2.520 cDPA. Each figure represents a relaxation step of 0.001 cDPA. At the bottom part of the first few frames, we can see a large defect, indicated by atoms with high VMS. In the later frames this high stress region is relaxed. The defected atomic configuration has been perturbed by a small incremental dose. This has destabilised its structure, allowing the atoms to rapidly reconfigure into a lower stress configuration in this region. It is incorrect to conclude that an interstitial defect cluster has diffused to and been absorbed into a GB 'sink' in this sequence of images. Instead, it is appropriate to say that the local atomic configuration rearranged and attained a lower stress state. This sequence of images shows that interfaces between relatively disordered high-energy-per-atom and relatively perfect crystalline regions act as recycling areas catalysing the recombination of defects. GBs do *not* act as sinks for defects, they are catalysts for recombination, and this study reveals the microscopic mechanism of how this actually happens.

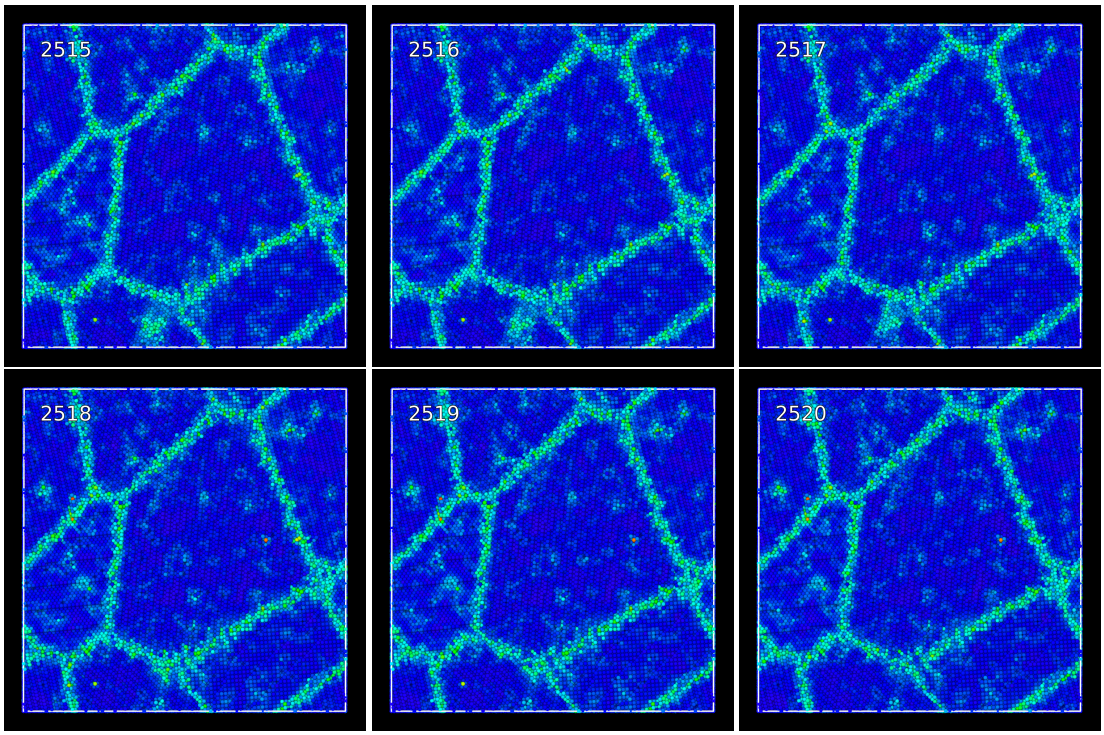

Figure 10. The von Mises stress of a sample with initial d_c=10.0 nm at a dose of 2.515 to 2.520 cDPA, corresponding to relaxation step 2515 to 2520. A defect cluster at the bottom part of each figure is absorbed by GB. Same colour coding as in Fig. 8.

4. Conclusions

We observe that nanocrystalline tungsten is more resistant to swelling under the high irradiation dose, low temperature conditions, using atomistic simulations performed with the Creation-Relaxation Algorithm. Irradiation causes damage and generates lattice defects, but GBs absorb defects through continuous rearrangement of their local atomic configurations, leading to the formation of denuded zones near GBs. This also changes the morphology of grain boundaries, causing grain coarsening. Even without thermally driven defect diffusion, the GB-defect interaction elucidated in this work occurs through spatial energy minimisation, which is the origin of the movements and fluctuations of the GBs. In reality, with thermal activation included, the physical origin of these effects cannot disappear- rather the fluctuating stresses will act to reduce some activation barriers to atomic rearrangement. The total defect concentration is lower in small grained systems, because the relative volume corresponding to denuded zones is larger. The excess volume due to the GBs is also lower, due to the lower GB area. These explain the lower swelling in NC materials. In contrast to previous works using single crystal simulations, we do not attain a dynamically fluctuating steady state in the potential energy of NC tungsten up to 2.5 cDPA, because the transient changes in the GB area take longer than the accumulation of defects.

Acknowledgement(s)

This work has been carried out within the framework of the EUROfusion Consortium, funded by the European Union via the Euratom Research and Training Programme (Grant Agreement No 101052200 — EUROfusion) and from the UK EPSRC Energy Programme (grant number EP/W006839/1), and was partially supported by the Broader Approach Phase II agreement under the PA of IFERC2-T2PA02. To obtain further information on the data and models underlying the paper please contact PublicationsManager@ukaea.uk. Views and opinions expressed are however those of the authors only and do not necessarily reflect those of the European Union or the European Commission. Neither the European Union nor the European Commission can be held responsible for them. We gratefully acknowledge the provision of computing resources by the IRIS (STFC) Consortium.

Disclosure statement

No potential conflict of interest was reported by the author(s).

References

[1] Sato S, Maki K. Analytical representation for neutron streaming through slits in fusion reactor blanket by Monte Carlo calculation. Fusion Engineering and Design. 2003;65:501–524.

[2] Gilbert MR, Marian J, Sublet JC. Energy spectra of primary knock-on atoms under neutron irradiation. Journal of Nuclear Materials. 2015;467:121–134.

[3] Sand AE, Dudarev SL, Nordlund K. High-energy collision cascades in tungsten: Dislocation loops structure and clustering scaling laws. EPL (Europhysics Letters). 2013 aug; 103(4):46003. Available from: https://doi.org/10.1209%2F0295-5075%2F103%2F46003.

[4] Sand AE, Aliaga MJ, Caturla MJ, et al. Surface effects and statistical laws of defects in primary radiation damage: Tungsten vs. iron. EPL (Europhysics Letters). 2016 aug; 115(3):36001. Available from: https://doi.org/10.1209%2F0295-5075%2F115%2F36001.

[5] Mason DR, Sand AE, Yi X, et al. Direct observation of the spatial distribution of primary cascade damage in tungsten. Acta Materialia. 2018;144:905 – 917. Available from: http://www.sciencedirect.com/science/article/pii/S1359645417308893.

[6] Nordlund K, Zinkle SJ, Sand AE, et al. Improving atomic displacement and replacement calculations with physically realistic damage models. Nature Communications. 2018; 9:1084.

[7] Hofmann F, Mason DR, Eliason JK, et al. Non-contact measurement of thermal diffusivity in ion-implanted nuclear materials. Scientific Reports. 2015 Nov;5. Available from: https://doi.org/10.1038/srep16042.

[8] Cui S, Doerner RP, Simmonds MJ, et al. Thermal conductivity degradation and recovery in ion beam damaged tungsten at different temperature. Journal of Nuclear Materials. 2018;511:141 – 147. Special Section on 18th International Conference on Fusion Reactor Materials; Available from: http://www.sciencedirect.com/science/article/pii/S002231151830494X.

[9] Reza A, Yu H, Mizohata K, et al. Thermal diffusivity degradation and point defect density in self-ion implanted tungsten. Acta Materialia. 2020;193:270–279. Available from: https://www.sciencedirect.com/science/article/pii/S1359645420302214.

[10] Odette GR, Lucas GE. Embrittlement of nuclear reactor pressure vessels. JOM. 2001; 53:18–22.

[11] Hasegawa A, Fukuda M, Nogami S, et al. Neutron irradiation effects on tungsten materials. Fusion Engineering and Design. 2014;89(7):1568 – 1572. Proceedings of the 11th International Symposium on Fusion Nuclear Technology-11 (ISFNT-11) Barcelona, Spain, 15-20 September, 2013; Available from: http://www.sciencedirect.com/science/article/pii/S0920379614003123.

[12] Matolich J, Nahm H, Moteff J. Swelling in neutron irradiated tungsten and tungsten-25 percent rhenium. Scripta Metallurgica. 1974;8(7):837–841. Available from: https://www.sciencedirect.com/science/article/pii/0036974874903044.

[13] Garner FA, Toloczko MB, Sencer BH. Comparison of swelling and irradiation creep behavior of fcc-austenitic and bcc-ferritic/martensitic alloys at high neutron exposure. Journal of Nuclear Materials. 2000;276(1):123–142. Available from: https://www.sciencedirect.com/science/article/pii/S0022311599002251.

[14] Holt RA. Mechanisms of irradiation growth of alpha-zirconium alloys. Journal of Nuclear Materials. 1988;159:310–338.

[15] Boutard JL, Alamo A, Lindau R, et al. Fissile core and tritium-breeding blanket: structural materials and their requirements. Comptes Rendus Physique. 2007;9:287–302.

[16] Cabet C, Dalle F, Gaganidze E, et al. Ferritic-martensitic steels for fission and fusion applications. Journal of Nuclear Materials. 2019;523:510–537.

[17] Gleiter H. Nanocrystalline materials. Progress in Materials Science. 1989;33(4):223–315. Available from: https://www.sciencedirect.com/science/article/pii/0079642589900017.

[18] Samaras M, Derlet PM, Van Swygenhoven H, et al. Computer simulation of displacement cascades in nanocrystalline ni. Phys Rev Lett. 2002 Mar;88:125505. Available from: https://link.aps.org/doi/10.1103/PhysRevLett.88.125505.

[19] Nita N, Schaeublin R, Victoria M. Impact of irradiation on the microstructure of nanocrystalline materials. Journal of Nuclear Materials. 2004;329–333:953–957.

[20] Beyerlein IJ, Caro A, Demkowicz MJ, et al. Radiation damage tolerant nanomaterials. Materials Today. 2013;16(11):443–449. Available from: https://www.sciencedirect.com/science/article/pii/S1369702113003581.

[21] Dürrschnabel M, Klimenkov M, Jäntsch U, et al. New insights into microstructure of neutron-irradiated tungsten. Scientific Reports. 2021 Apr;11(1):7572. Available from: https://doi.org/10.1038/s41598-021-86746-6.

[22] El-Atwani O, Suslova A, Novakowski T, et al. In-situ tem/heavy ion irradiation on ultrafine-and nanocrystalline-grained tungsten: Effect of 3mev si, cu and w ions. Materials Characterization. 2015;99:68–76. Available from: https://www.sciencedirect.com/science/article/pii/S104458031400343X.

[23] Rose M, Balogh A, Hahn H. Instability of irradiation induced defects in nanostructured materials. Nuclear Instruments and Methods in Physics Research Section B: Beam Interactions with Materials and Atoms. 1997; 127-128:119–122. Ion Beam Modification of Materials; Available from: https://www.sciencedirect.com/science/article/pii/S0168583X96008634.

[24] Dey S, Drazin JW, Wang Y, et al. Radiation tolerance of nanocrystalline ceramics: Insights from yttria stabilized zirconia. Scientific Reports. 2015 Jan;5(1):7746. Available from: https://doi.org/10.1038/srep07746.

[25] Zhu Y, Luo J, Guo X, et al. Role of grain boundaries under long-time radiation. Phys Rev Lett. 2018;120:222501.

[26] Tschopp MA, Solanki KN, Gao F, et al. Probing grain boundary sink strength at the nanoscale: Energetics and length scales of vacancy and interstitial absorption by grain boundaries in α-fe. Phys Rev B. 2012 Feb;85:064108. Available from: https://link.aps.org/doi/10.1103/PhysRevB.85.064108.

[27] Bai XM, Voter AF, Hoagland RG, et al. Efficient annealing of radiation damage near grain boundaries via interstitial emission. Science. 2010;327(5973):1631–1634. Available from: https://science.sciencemag.org/content/327/5973/1631.

[28] Jin M, Cao P, Yip S, et al. Radiation damage reduction by grain-boundary biased defect migration in nanocrystalline cu. Acta Materialia. 2018;155:410–417. Available from:

https://www.sciencedirect.com/science/article/pii/S1359645418304622.
[29] Jin M, Cao P, Short MP. Mechanisms of grain boundary migration and growth in nanocrystalline metals under irradiation. Scripta Materialia. 2019;163:66–70. Available from: https://www.sciencedirect.com/science/article/pii/S1359646219300077.
[30] Li X, Liu W, Xu Y, et al. Radiation resistance of nano-crystalline iron: Coupling of the fundamental segregation process and the annihilation of interstitials and vacancies near the grain boundaries. Acta Materialia. 2016;109:115–127. Available from: https://www.sciencedirect.com/science/article/pii/S1359645416301021.
[31] Kaoumi D, Motta AT, Birtcher RC. A thermal spike model of grain growth under irradiation. Journal of Applied Physics. 2008;104:073525.
[32] Wang P, Thompson DA, Smeltzer WW. Implantation of Ni thin films and single crystals with Ag ions. Nuclear Instruments and Methods in Physics Research Section B: Beam Interactions with Materials and Atoms. 1985;7–8:97–102.
[33] Wang P, Thompson DA, Smeltzer WW. Implantation and grain growth in Ni thin films induced by Bi and Ag ions. Nuclear Instruments and Methods in Physics Research Section B: Beam Interactions with Materials and Atoms. 1986;16:288–292.
[34] Bufford DC, Abdeljawad FF, Foiles SM, et al. Unraveling irradiation induced grain growth with in situ transmission electron microscopy and coordinated modeling. Appl Phys Lett. 2015;107:191901.
[35] Vineyard GH. Thermal spikes and activated processes. Radiation Effects. 1976;29:245–248.
[36] Levo E, Granberg F, Utt D, et al. Radiation stability of nanocrystalline single-phase multicomponent alloys. Journal of Materials Research. 2019;34(5):854–866.
[37] Granberg F, Byggmästar J, Nordlund K. Molecular dynamics simulations of high-dose damage production and defect evolution in tungsten. Journal of Nuclear Materials. 2021;556:153158. Available from: https://www.sciencedirect.com/science/article/pii/S0022311521003810.
[38] Derlet PM, Dudarev SL. Microscopic structure of a heavily irradiated material. Phys Rev Materials. 2020 Feb;4:023605. Available from: https://link.aps.org/doi/10.1103/PhysRevMaterials.4.023605.
[39] Warwick AR, Boleininger M, Dudarev SL. Microstructural complexity and dimensional changes in heavily irradiated zirconium. Phys Rev Mater. 2021;5:113604.
[40] Mason DR, Das S, Derlet PM, et al. Observation of transient and asymptotic driven structural states of tungsten exposed to radiation. Phys Rev Lett. 2020 Nov;125:225503. Available from: https://link.aps.org/doi/10.1103/PhysRevLett.125.225503.
[41] Chartier A, Marinica MC. Rearrangement of interstitial defects in alpha-fe under extreme condition. Acta Materialia. 2019;180:141–148. Available from: https://www.sciencedirect.com/science/article/pii/S1359645419305877.
[42] Wang S, Guo W, Schwarz-Selinger T, et al. Dynamic equilibrium of displacement damage defects in heavy-ion irradiated tungsten. Acta Materialia. 2022;:118578Available from: https://www.sciencedirect.com/science/article/pii/S1359645422009533.
[43] Federici G, Boccaccini L, Cismondi F, et al. An overview of the eu breeding blanket design strategy as an integral part of the demo design effort. Fusion Engineering and Design. 2019;141:30–42. Available from: https://www.sciencedirect.com/science/article/pii/S0920379619301590.
[44] You JH, Visca E, Bachmann C, et al. European DEMO divertor target: Operational requirements and material-design interface. Nuclear Materials and Energy. 2016;9:171–176. Available from: http://dx.doi.org/10.1016/j.nme.2016.02.005.
[45] Hirel P. Atomsk: A tool for manipulating and converting atomic data files. Computer Physics Communications. 2015;197:212–219. Available from: https://www.sciencedirect.com/science/article/pii/S0010465515002817.
[46] Plimpton S. Fast parallel algorithms for short-range molecular dynamics. Journal of Computational Physics. 1995;117(1):1–19. Available from: https://www.sciencedirect.com/science/article/pii/S002199918571039X.

[47] http://lammps.sandia.gov ; ????
[48] Marinica MC, Ventelon L, Gilbert MR, et al. Interatomic potentials for modelling radiation defects and dislocations in tungsten. Journal of Physics: Condensed Matter. 2013 sep;25(39):395502. Available from: https://doi.org/10.1088%2F0953-8984%2F25%2F39%2F395502.
[49] Mason DR, Nguyen-Manh D, Becquart CS. An empirical potential for simulating vacancy clusters in tungsten. Journal of Physics: Condensed Matter. 2017 nov;29(50):505501.
[50] Norgett M, Robinson M, Torrens I. A proposed method of calculating displacement dose rates. Nuclear Engineering and Design. 1975;33(1):50–54. Available from: https://www.sciencedirect.com/science/article/pii/0029549375900357.
[51] Ma PW, Dudarev SL. Symmetry-broken self-interstitial defects in chromium, molybdenum, and tungsten. Phys Rev Materials. 2019 Apr;3:043606. Available from: https://link.aps.org/doi/10.1103/PhysRevMaterials.3.043606.
[52] Mason DR, Granberg F, Boleininger M, et al. Parameter-free quantitative simulation of high-dose microstructure and hydrogen retention in ion-irradiated tungsten. Phys Rev Materials. 2021 Sep;5:095403. Available from: https://link.aps.org/doi/10.1103/PhysRevMaterials.5.095403.
[53] Mohamed W, Miller B, Porter D, et al. The role of grain size on neutron irradiation response of nanocrystalline copper. Materials. 2016;9(3). Available from: https://www.mdpi.com/1996-1944/9/3/144.
[54] Barr CM, El-Atwani O, Kaoumi D, et al. Interplay between grain boundaries and radiation damage. JOM. 2019 Apr;71(4):1233–1244. Available from: https://doi.org/10.1007/s11837-019-03386-y.
[55] Barr CM, Chen EY, Nathaniel JE, et al. Irradiation-induced grain boundary facet motion: In situ observations and atomic-scale mechanisms. Science Advances. 2022;8(23):eabn0900. Available from: https://www.science.org/doi/abs/10.1126/sciadv.abn0900.
[56] Stukowski A, Bulatov VV, Arsenlis A. Automated identification and indexing of dislocations in crystal interfaces. Model Simul Mater Sci Eng. 2012;20:085007.
[57] Tian J, Wang H, Feng Q, et al. Heavy radiation damage in alpha zirconium at cryogenic temperature: A computational study. Journal of Nuclear Materials. 2021;555:153159. Available from: https://www.sciencedirect.com/science/article/pii/S0022311521003822.
[58] Ester M, Kriegel HP, Sander J, et al. A density-based algorithm for discovering clusters in large spatial databases with noise. In: Proceedings of the Second International Conference on Knowledge Discovery and Data Mining. AAAI Press; 1996. p. 226–231.
[59] Larsen PM, Schmidt S, Schiøtz J. Robust structural identification via polyhedral template matching. Modelling and Simulation in Materials Science and Engineering. 2016 may; 24(5):055007. Available from: https://dx.doi.org/10.1088/0965-0393/24/5/055007.
[60] Lorensen WE, Cline HE. Marching cubes: A high resolution 3d surface construction algorithm. In: Proceedings of the 14th Annual Conference on Computer Graphics and Interactive Techniques; New York, NY, USA. Association for Computing Machinery; 1987. p. 163–169; SIGGRAPH '87. Available from: https://doi.org/10.1145/37401.37422.
[61] Chernyaev E. Marching cubes 33 : Construction of topologically correct isosurfaces : Presented at graphicon '95 saint-petersburg russia 03-07.07.1995. CERN. Geneve. Computing and Networks Division; 1995. Graphicon 95.
[62] Stukowski A. Visualization and analysis of atomistic simulation data with ovito-the open visualization tool. Modelling and Simulation in Materials Science and Engineering. 2010 JAN;18(1).

Appendix

Finding grains and grain boundaries

This work makes use of the distance to a specified GB. In this section we will summarise the algorithms used to determinine whether an atom is in a particular grain, and how we find its distance to the GB.

The assignment of a grain index to each atom is based on the DBSCAN algorithm[58], and considers the orientation mismatch between each atom and its near neighbours. This assignment algorithm has three stages. Firstly, the crystal lattice orientation is determined for each atom. If we write the expected position of the kth neighbouring atom in the perfect lattice as $\vec{x}_k^0$, and the observed position as $\vec{x}_k^0$ we can minimise the fitting function $S = \sum_k (\mathbf{T}\vec{x}_k - \vec{x}_k^0 - \vec{\delta})^2$, with repect to the nine components of the deformation gradient matrix $\mathbf{T}$ and the vector displacement $\vec{\delta}$. While this algorithm is known to be less efficient than the graph-based Polyhedral Template Matching algorithm[59], it is more robust when there are many lattice defects. We choose to fit to the expected neighbour positions within 1.5 lattice parameters, which is between third and fourth nearest neighbour shells for bcc. We interpret the deformation gradient as a stretch and rotation, $\mathbf{T} = (1+\varepsilon)\mathbf{R}$ using the polar decomposition method, and find a quaternion representing the local lattice rotation $\mathbf{R}$.

For the second step, regions where clusters of atoms have similar orientations to their neighbours are identified. These regions are the grain interiors. This is done by finding the quaternion distance between two neighbouring atoms, $d = 1 - (q_1 \cdot q_2)^2$, which gives the angle of rotation, θ, between two atom orientations as $\cos\theta = 1 - 2d$. Each atom for which $\theta < \theta_{max}$ for every neighbour is in a crystalline region. The other atoms form an unsorted pile. We choose $\theta_{max} = 5°$. These are clustered so that two atoms within a distance r_c of each other in a crystalline region are assigned to the same grain, g, if the angle between them $\theta < \theta_{max}$. We chose $r_c = 1.1$ lattice parameters.

As the third and final step of the assignment algorithm, the atoms in the unsorted pile (non-crystalline) are adopted into grains where possible. We first return to the pile any atom already assigned to grain g, if the majority of its neighbours (distance within r_c) are in a different grain g'. Then we assign any atom on the pile to grain g if it has a close orientation ($\theta < \theta_{max}$) to a majority of neighbours already in grain g. Then we assign any atom on the pile to grain g if it has a simple majority of neighbours already in grain g. Lastly we return all atoms in a grain with fewer than N_{min} atoms to the pile. We choose $N_{min} = 100$. This process of unassigning and reassigning to adopt atoms into grains is iterated until a stable grain distribution is found. Some atoms will never be assigned to a grain if no majority can be found.

While the algorithm above will place nearly all atoms into grains, even when there is a large number of lattice defects, it does not define the grain *boundaries*. We use the definition that the GB is a hypothetical surface dividing two crystalline regions with different orientations. This definition does not preclude the possibility that there exists a volume near the surface which is amorphous, nor does it preclude a void or precipitate straddling the surface.

If a GB is so defined, then a computationally efficient representation of it is a triangulated surface. Using a triangulated surface, the subsequent calculations we need are simple - the volume enclosed and the area are well defined, as is the distance of any point to the nearest triangle on the surface.

In order to compute the GB surfaces, we start with the atom positions and their assigned grain indices, as computed above. We then define a regular spaced node lattice

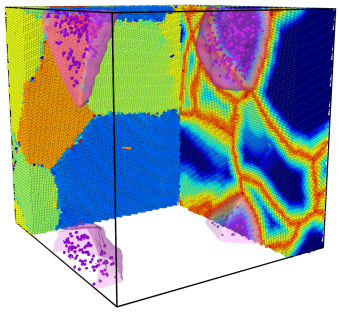

Figure 11. A 30 grain nanocrystalline sample at dose 2.5 cDPA analysed using the methods described here. Atoms on the back left face coloured by orientation. Atoms on back right face coloured by distance to grain boundary. Pink surface shows the triangulated surface constructed for one grain, and purple surfaces show voids within this grain. Image rendered using data exported to Ovito [62].

with spacing L chosen to be greater than the lattice parameter and smaller than the expected radius of curvature of the grains. For this work we chose $L = 5\mathring{A}$, but the result is insensitive to the exact choice. Each node is at the centre of a roughly cubic cell containing several atoms. We consider the positions and grain index of all atoms within the neighbouring 27 cells of a node point. For each pair of grains, g, g', we fit an assumed phase parameter profile $\phi_{g,g'}(\vec{x}) = \tanh(\vec{x} \cdot \vec{b}_{g,g'} + a_{g,g'})$, which minimises the function

$$S_{g,g'} = \sum_{i,g_i=g} \left(\phi(\vec{\delta x}_i) - 1\right)^2 + \sum_{i,g_i=g'} \left(\phi(\vec{\delta x}_i) + 1\right)^2 + \left(\frac{1}{|\vec{b}_{g,g'}|} - L\right)^2, \quad (1)$$

where $\vec{\delta x}_i$ is the vector to atom i in grain g or g' from the node. This will return a vector $\vec{b}_{g,g'}$ normal to the plane dividing atoms of type g and g', oriented such that $\phi = +1$ in grain g, and $\phi = -1$ in grain g', and the last term stops the interface becoming infinitely sharp. The position across the $g - g'$ GB at the node point is $\phi_{g,g'}(\vec{0}) = \tanh(a_{g,g'})$.

With the phase parameter position across each of the GBs computed at each node, the extent to which the node is in grain g is the value $\phi_g = \min(\{\phi_{g,g'}\})$, which takes the value -1 for a point deep inside grain g, and the value $+1$ for a point far outside grain g. We can (tri)linearly interpolate this function to find a phase field at every point in space, such that $\phi_g(\vec{x})$ returns the correct values on the nodes, and so a triangulated surface for the boundary of grain g can then be readily found as the isosurface $\phi_g(\vec{x}) = 0$ using the Marching Cubes algorithm[60,61].

An illustration of the result of this method is shown in figure 11. We can see a few GB atoms and defects with local lattice orientations proving difficult to identify, but a constant orientation in grains is produced by the slow but robust method described above. One grain is shown as a triangulated surface, within which vacancies are drawn using the isosurface method of [52]. Note that a denuded zone is clearly visible.

It is our intention to release the GB code simultaneously with this paper and place the link here.